Augmented Structure Preserving Neural Networks for cell biomechanics

Juan Olalla-Pombo[a], Alberto Badías[a], Miguel Ángel Sanz-Gómez[a], José María Benítez[a], Francisco Javier Montáns[a,b]

[a] *E.T.S. de Ingeniería Aeronáutica y del Espacio, Universidad Politécnica de Madrid, Plaza del Cardenal Cisneros, 3, Madrid, 28040, Spain*
[b] *Department of Mechanical and Aerospace Engineering, Herbert Wertheim College of Engineering, University of Florida, Gainesville, FL 32611, USA*

Abstract

Cell biomechanics involve a great number of complex phenomena that are fundamental to the evolution of life itself and other associated processes, ranging from the very early stages of embryo-genesis to the maintenance of damaged structures or the growth of tumors. Given the importance of such phenomena, increasing research has been dedicated to their understanding, but the many interactions between them and their influence on the decisions of cells as a collective network or cluster remain unclear. We present a new approach that combines Structure Preserving Neural Networks, which study cell movements as a purely mechanical system, with other Machine Learning tools (Artificial Neural Networks), which allow taking into consideration environmental factors that can be directly deduced from an experiment with Computer Vision techniques. This new model, tested on simulated and real cell migration cases, predicts complete cell trajectories following a roll-out policy with a high level of accuracy. This work also includes a mitosis event prediction model based on Neural Networks architectures which makes use of the same observed features.

Keywords: Cell migration, Computer Vision, Tracking, Machine Learning, Structure Preserving Neural Networks

1. Introduction

Cell migration mechanisms are known to be present in many fundamental processes throughout the evolution of living organisms. From the creation of

life through embryogenesis [1, 2] to the growth and reparation of tissue structures or the evolution of tumors [3, 4, 5], the movement of cells is necessary, and the collective patterns followed by cell networks and clusters determine not only the kinetics but also the results of these processes.

As cells are living units that perform complex tasks, undergo constant reactions and transformations, interact with other cells and can respond to their surroundings, their migration can be presented as the result of a large number of internal and external factors. The influence of many environmental factors such as chemical gradients that can be created with biomaterials [6] or that might appear in organic environments [7], density gradients caused by cell accumulation [8], or even the presence of dead cells (which can be of interest in wound healing or tumor growth processes) [9] has been thoroughly studied. Other external factors related to cell collective movement and the tensile forces that can appear between them have also been analyzed [10, 11], with several works in this field showing that cells can use protuberances to attach themselves to other cells, which later exert pulling or pushing forces to guide their movement [12].

Despite the precision that the proposed models can achieve while explaining the relation between these factors and cell movements, there is a general lack of a global approach to the problem. Due to the possible interrelations between environmental properties, many studies simplify the problem by creating conditions where the studied gradient or feature is the dominant source of instability, and thus the main reason behind cell migration [13]. This often requires the design of *in vitro* experiments that take place in synthetic environments that aim to resemble organic conditions [14]. However, the environmental conditions inside living beings or surrounding single-cell organisms are complex and encompass a large number of gradients (nutrients, oxygen, or other types of chemical variation) [15], which cause cells to follow different trends of movement. The number of *in vivo* experiments is scarce, due to their execution complexity and the rapid development of *in vitro* techniques [16], which impedes a proper understanding of the complete underlying mechanisms of cell migration. In these cases, it can be difficult to correctly assess the magnitude of the gradients or possible interactions between cells, resulting in high levels of uncertainty in the observations.

To overcome these issues, we present a new approach that aims to understand cell migration mechanisms as a whole, making use of Machine Learning (ML) techniques. ML algorithms allow pattern detection in large sets of data and can handle interrelated features that influence one another. Thus, their

application to complex and fluctuating problems (such as organic environments) is becoming more common. Extensive efforts have been made in the fields of tissue engineering, where these methods can help predict cell behavior and development [17]. Some works have even applied Deep Learning (DL) networks to cell migration problems. García-Moreno *et al.* [18] propose recurrent and convolutional network architectures to study the migration mechanisms of breast cancer cells in the context of wound healing. Their work has been tested on *in vivo* cases that showcase the ability of this type of techniques to reproduce complex trajectories. Other studies have also used ML techniques to adjust known physical phenomena that participate in cell migration processes (such as nematic mechanisms or hydrodynamic effects [19]). Even if these results have been validated and are a promising tool to predict tissue evolution and cell movement, they do not provide as much information on the underlying physical mechanisms due to the opacity of recurrent units. These models used a supervised learning approach that focuses on the minimization of a loss function, without taking into account the compliance with any physical principle. Whereas forcing the compliance of experimental data with adjusted laws of kinematics and dynamics can be a reduced approach that oversees a great number of physical and biological effects that influence cells, biomechanical systems must still comply with universal principles such as the laws of thermodynamics.

In this context, we propose a hybrid model that combines Structure Preserving Neural Networks (SPNN) with Multi Layer Perceptrons (MLP), named Augmented Structure Preserving Neural Networks (ASPNN). Its objective is to predict cell velocities for a given moment in time and entire trajectories following a *roll-out* policy (meaning that the position of the cell is only provided to the model as data in the first frame) given a series of inputs related to cell state and surrounding conditions. The SPNN studies the problem from a purely mechanical standpoint, and allows compliance of the system with thermodynamical principles: conservation of total energy and increasing entropy. This submodel focuses on the deep analysis of the energetic behavior of the system, allowing the detection of external sources of energy, such as chemical gradients of some kind. However, as mentioned before, cell migration problems include a series of factors that extend beyond the mechanical domain and are related to cellular responses to external cues. Many of said factors can be controlled or observed in *in vitro* experiments, such as some chemical or density gradients [20], but are not always defined *in vivo*. However, some cannot be continuously observed, such as the degree

of attachment between cells (some studies measure it qualitatively by stress maps on a substrate [21] or visual analysis of shape and area variations [22]). Cell systems are thus not completely observable, which forces the application of a different tool that allows underlying pattern detections. Our MLP aims to learn the influence of external factors beyond purely mechanical events (such as elastic collisions) on the migration behavior of cells. The low level of comprehensibility of the learning process of this architecture is aligned with the inherent complexity of the biological processes that take place.

With this approach, we combine explainable studies of a physical system that complies with basic principles with a detailed analysis of a large number of factors simultaneously, eliminating the need for *ad hoc* crafted environments that highlight a given gradient or external stimuli. Moreover, the model presented only uses features that can be obtained from a video or a set of images as input. These features are extracted by means of Computer Vision (CV) techniques for image segmentation and object tracking. That allows its application to *in vivo* environments and experiments, since there is no need for additional data. Hence, we propose a general method that allows noninvasive (visual observations can serve as input) *in vivo* analysis of cell migration from a global point of view, with a high degree of explainability. This model has been tested on synthetic cases and a real *in vitro* experiment. Furthermore, we present a mitotic event prediction model to determine the probability of a cell to undergo a mitotic process given its current state and environmental cues (using the same features as the ASPNN). In this regard, some studies have focused on the detection, analysis, and recognition of mitotic events using DL with high precision results (see the work by Mao *et al.* [23] or Delgado-Rodríguez *et al.* [24]), but very few have explored the predictive task. Having the ability to correctly predict division events would allow better understanding and forecasting of the evolution of rapidly growing systems, such as tumor environments, where the mitotic rate can be a defining parameter [25].

The data acquisition and processing process is described in Section 2, while Section 3 contains a discussion of the results, and final comments are included in Section 4.

2. Materials and Methods

This section includes a general overview of the process for data acquisition and the creation of the neural model architecture.

2.1. Data processing and feature extraction

The input for our ASPNN is directly a video sequence, that has to be divided consecutive frames. A Segment Anything Model (SAM) [26] architecture was used to segment the image, locate and create a mask for each cell on the frame. Image segmentation was the preferred alternative over other methods of cell location, such as object detection because the extracted information about the shape and size of the cell was deemed of interest to characterize its behavior (e.g., cells usually undergo shape variations when starting mitosis processes). Frame images first underwent a series of preprocessing modifications, such as the application of median blur filters to eliminate noise [27], Wiener deconvolution filters to increase resolution [28], or grayscale. Table 1 shows the data obtained from segmentation.

Table 1: Data to be obtained for each cell and frame in the segmentation stage.

Parameter	**Comments**
Cell ID Number	Automatically assigned
Segmentation Mask	Stored in Run-Length Enconding (RLE) format
Cell Area	Number of pixels covered by the mask
Eccentricity	Cells are approximated to elliptical bodies
Predicted Intersection over Union (IoU)	To be used as predicted accuracy to discard incorrect segmentations
Stability Score	Confidence score value

After optimization of a number of parameters (mainly predicted Intersection over Union threshold and stability score threshold), SAM models showed great results in cell segmentation, recognizing cells with very low levels of brightness or separating clusters of several of them with diffused cell borders (see Figure 1).

As a requirement of the tracking algorithms, the bounding boxes were also calculated for each cell mask, using the maximum and minimum horizontal and vertical coordinates to determine its limits. In this case, IoU threshold values between bounding boxes were included so that cells in clusters could be

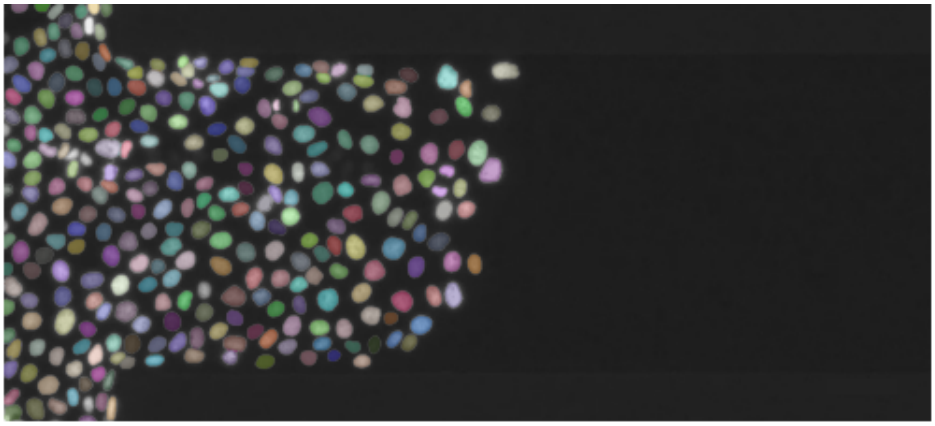

Figure 1: Segmented image with masks represented as colored layers over cells in the frame.

efficiently detected and separated. During the first tests, additional bounding boxes were created around the entire clusters. In addition, only cells located within the vertical limits of the microchannel and at a 50 pixel distance from the left border of the image were considered, to avoid partially visible cells or those that enter and exit the frame, which could distort the function of the tracking algorithms (they were included in images, but data from those bounding boxes were discarded).

Once cells have been detected and segmented in each of the frames, their trajectories must be tracked to gain understanding of their movement. This poses a complex problem due to the high number of cells in the channel, their *a priori* high variability movement, and the similarities between them, which makes differentiation tasks (based on size and shape) difficult. After several preliminary tests, the selected tracking algorithm was DeepOCSort [29] with ReIdentification (ReID) models. This algorithm, based on OC-Sort [30], uses Kalman Filters and ReIdentification models based on visual features to associate objects in subsequent frames. The model had to be finely tuned to correctly track cells along the sequence. General Intersection over Union (GIoU) was the preferred association function, with threshold levels of 0.05 for the addition of a mask to a given trajectory. Recovery parameters were also included; for example, if a given trajectory ends due to the lack of suitable candidates in a frame, candidates will still be searched for in the following 4 frames. This was found to be useful for correctly tracking objects in the limits of the microchannel. The general tendency was to allow

low-confidence detection of a large number of trajectories, which have later been filtered on the basis of stability, length, and visual correlation with the image sequence. Table 2 shows data obtained from the tracking algorithm.

Table 2: Data to be obtained for each cell and frame in the tracking stage.

Parameter	**Comments**
Bounding Box Limits	Coordinates of top-left and bottom-right corners
ID Number	For trajectory identification
Confidence	For trajectory filtering
Frame Number	Later used for data classification

After filtering the trajectories (eliminating those with fewer than 5 frames), a total of 566 different trajectories were obtained. Other filters were applied in subsequent stages, since some new trajectories might have been created due to mitotic events or loss of a given cell during a series of frames. Trajectories data were then grouped by trajectory and by frame, which was useful to later determine environmental conditions (such as number of surrounding cells) for a cell in a given frame.

After data were collected for cell trajectories, a number of features were extracted directly from cell positions and shape parameters (area and eccentricity). These features will then be used as input to the ASPNN. Given the structure of the model, only trajectories with more than 105 frames were considered correct trajectories (for data encapsulation matters, only the first 105 frames were studied for these trajectories). Data from the rest of the cells were still used to calculate environmental characteristics. For every frame of each of the correct trajectories, Table 3 shows the obtained features.

Table 3: Features obtained for each frame of the correct trajectories.

Feature	**Comments**
Cell center coordinates	x and y coordinates

Table 3 continued from previous page

Cell velocity	In x and y directions, calculated as the difference between the center coordinates of the cell in subsequent frames.
Density gradient	Calculated from the collective area of cells located in a 8 20-pixel square grid surrounding the cell.
Cell density in each grid square	8 values corresponding to the density of cells on each region.
Number of surrounding cells	Calculated as the number of cells with center coordinates within 75 pixels of the cell.
Number of cells per sector	The images have been divided into 4 different sectors (top left, top right, bottom left, and bottom right). The number of cells in each sector provides data on the general distribution of cells and free space.
Average velocity of surrounding cells	In x and y directions.
Cell brightness value	Obtained directly from the grayscale images.
Cell area variation	Difference in cell area in subsequent frames.
Cell eccentricity	

These parameters would later be divided into output (cell velocity) and input (all remaining features), resulting in vectors of size 23 and 2, respectively, for each frame of each correct trajectory.

2.2. ASPNN model

Our Augmented Structure Preserving Neural Network consists of two parts: a structure preserving model based on the General Equation for the Nonequilibrium Reversible-Irreversible Coupling, commonly referred to as

GENERIC [31], and an MLP model, named CoNN (Correction Neural Network), considering environmental conditions surrounding the cell.

2.2.1. GENERIC submodel

GENERIC algorithm defines a problem structure based on two "potentials", total energy (E) and entropy (S). With this definition, the mechanical problem can be divided into reversible and irreversible dynamics. Reversible dynamics are contemplated within the context of total energy conservation (energy term), whereas irreversible dynamics is governed by the imposed increase in entropy. Each of the potentials is linked to a matrix that contains the relations between the observable variables of the system. For a system with a set of observable variables z, the evolution of said variables over time can be calculated with

$$\frac{d\mathbf{z}}{dt} = L\frac{\partial E}{\partial \mathbf{z}} + M\frac{\partial S}{\partial \mathbf{z}} \ , \tag{1}$$

where L and M are the linear operators related to total energy and entropy, respectively, and which must comply with the following degeneracy conditions to ensure thermodynamical consistency:

$$L\frac{\partial S}{\partial \mathbf{z}} = 0 \ , \tag{2}$$

$$M\frac{\partial E}{\partial \mathbf{z}} = 0 \ . \tag{3}$$

The structure of both matrices will depend on the structure of the problem, but they can usually be derived from the literature or, for conservative systems, can be constructed from resulting equations of Hamiltonian mechanics applied to the system. However, these matrices might be unknown for complex non-observable systems with irreversible terms.

Within the theoretical framework of GENERIC, many different numerical methods for mechanical analysis have emerged during the past years. In this context, the work by Romero [32] is of great interest. The author proposes time-stepping algorithms that allow propagation of the state of a system over time, which leads to the characterization of its mechanical behavior. These integrating algorithms allow for the transformation of the problem into a set of discrete time steps by means of finite differences, so that Equation 1 translates to

$$\frac{\mathbf{z}_{n+1} - \mathbf{z}_n}{\Delta t} = L \cdot \frac{\mathrm{D}E}{\partial \mathbf{z}} + M \cdot \frac{\mathrm{D}S}{\partial \mathbf{z}} \ , \tag{4}$$

where $\mathrm{D}E$ and $\mathrm{D}S$ are the discrete gradients of both potentials.

Over the past few years, many efforts have been guided towards the combination of the GENERIC framework and Deep Learning. While providing general rules for the evolution of mechanical systems, they can be adapted to complex systems where the exact governing mechanisms are not exactly known, as they must still be thermodynamically consistent. The authors of this manuscript have studied the possible applications of this combination in previous work [33]. Their major contribution is the new definition of discrete energy and entropy gradients in terms of a gradient matrix, based on a finite element approach,

$$\frac{\mathrm{D}E}{\partial \mathbf{z}} \simeq A\mathbf{z} \ , \tag{5}$$

$$\frac{\mathrm{D}S}{\partial \mathbf{z}} \simeq B\mathbf{z} \ , \tag{6}$$

so that the resulting equation for the evolution of the system would be

$$\frac{\mathbf{z}_{n+1} - \mathbf{z}_n}{\Delta t} = L \cdot A\mathbf{z} + M \cdot B\mathbf{z} \tag{7}$$

and degeneracy conditions result in

$$L \cdot B\mathbf{z} = 0 \tag{8}$$

$$M \cdot A\mathbf{z} = 0 \tag{9}$$

where A and B are gradient matrices of which the structure is determined to adapt to the structure of the problem during the learning process. By learning these two matrices, the model is learning the underlying physics of the problem (relations between observable variables and energy and entropy variations) while ensuring compliance with thermodynamical laws. The model structures proposed in this study are based on those presented in the cited work.

Thus, the first part of the ASPNN consists of a MLP which will output the corresponding A and B matrices. For the training process, a loss function that encompasses both the correct prediction of state variables and the

correct evolution of thermodynamical potentials in following time-steps has been defined. This loss function (l_t) is calculated by a linear combination of data loss (l_{data}), which will compare the prediction of the entire ASPNN with the ground truth by

$$l_{data} = (\mathbf{z}_{pred} - \mathbf{z}_{gt})^2 \tag{10}$$

where $\mathbf{z}_{pred}$ and $\mathbf{z}_{gt}$ are predicted and ground truth values for state variables, respectively; and degeneracy loss (l_{deg}), calculated as

$$l_{deg} = ||L \cdot B_{pred}\mathbf{z}_{pred}||_2^2 + ||M \cdot A_{pred}\mathbf{z}_{pred}||_2^2 \tag{11}$$

which results in

$$l_t = \lambda_d l_{data} + l_{deg} \ , \tag{12}$$

where λ_d is a tunable parameter that will be adjusted depending on the magnitude of each of the loss terms.

Our SPNN takes the position (size 2 vector with coordinates x and y) and the velocities ($\dot{x}$ and $\dot{y}$), which results in a vector of input variables of size 4. For this set of variables, L matrix, which must be skew-symmetric, is defined [32]:

$$L = \begin{bmatrix} 0 & 0 & 1 & 0 \\ 0 & 0 & 0 & 1 \\ -1 & 0 & 0 & 0 \\ 0 & -1 & 0 & 0 \end{bmatrix} \tag{13}$$

As for the matrix M, which is required to be symmetric and positive semi-definite (to ensure positive entropy variations), it has been defined as

$$M = \begin{bmatrix} 1 & -0.5 & 0 & 0 \\ -0.5 & 1 & 0 & 0 \\ 0 & 0 & 1 & -0.5 \\ 0 & 0 & -0.5 & 1 \end{bmatrix} \tag{14}$$

to account for possible dissipation related to cell position and velocity (friction due to viscous effects) in both coordinates (which can be intertwined, thus the -0.5 terms outside of the main diagonal).

This SPNN GENERIC-based architecture will output a new set of variables for each time-step (position and velocity in the following frame). The

model is based on a fully connected architecture with 5 hidden layers with $16, 64, 128, 64$ and 16 neurons. Every layer uses hyperbolic tangent activation functions for smooth derivability. In order to maximize its range, inputs have been normalized to a $[-1, 1]$ interval

$$x_{norm} = 2 \cdot \frac{x - \max(x)}{\max(x) - \min(x)} - 1 \ . \tag{15}$$

2.2.2. CoNN submodel

The resulting velocities will then be combined with the aforementioned MLP model considering environmental characteristics. The final cell velocity will be obtained from the combination (with a multineuron layer) of both velocities. This velocity will then be used to calculate the new position of the cell (which will then be used as input in the next frame), following a *roll-out* policy. The complete process pipeline is shown in Figure 2.

This part of the model encompasses a fundamental part of the complexity of the underlying physical phenomena involved in cell migration, which is a process that surpasses the purely mechanical realm and is guided and influenced by surrounding conditions and gradients. This combination of responses to the external environment by the cell does not fully follow the physical properties of simple systems due to the large number of actors and internal mechanisms taking place. Thus, in order to fully understand the overall behavior of the system, an additional element with the ability to learn without the thermodynamical constraints of the GENERIC model. Hence, this part of the model is responsible of absorbing the effect of the surroundings of the cell in its movement.

The complexity of the surroundings, which translates into high-variance input data, guides the size and importance of this part of the model, which has been set as a MLP due to the flexibility and simplicity of training of this kind of architecture. This allows robust learning processes that can be thoroughly controlled and guided despite the complexity of input data and their unclear relations with output data (cell kinematics).

The MLP model consists of a fully connected architecture with four hidden layers with 181, 297, 149 and 295 neurons. The number of layers for this model, as well as the number of neurons for each one and the learning rate have been optimized with a Bayesian Optimization and HyperBand (BOHB) algorithm, which tests a series of parameter sets to determine which minimizes the defined loss function [34].

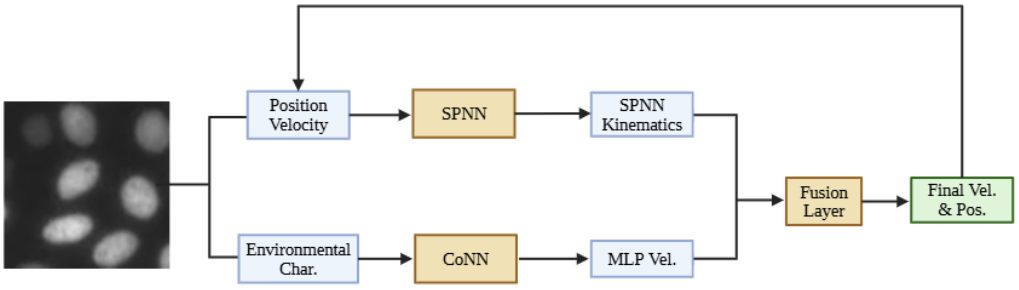

Figure 2: Complete process pipeline. Note that position and velocities inputs to the SPNN are only provided from the video in the first frame, with results from the model being used in subsequent frames.

The final MLP layer translates a set of 4 inputs (velocities from SPNN and MLP) into 2 final outputs. Although the weights and biases for this layer will still be updated during the learning process, its reduced size has made the strategy shift towards a conservative approach with low learning rates. All three parts of the model have been trained for 5000 epochs. The learning rates and learning rate scheduler parameters have been fine-tuned for each case, and are presented in the corresponding epigraphs of Section 3.

2.3. Mitosis prediction model

The mitosis prediction model also uses a MLP architecture with fully connected layers. It uses the same input as the ASPNN, that is, the position and velocity of a cell (also obtained from model results in previous frames, following the *roll-out* policy) and its surrounding conditions (environmental characteristics). In addition, two new inputs have been included, cell area and brightness variations over time. The reason for the introduction of these parameters was the visual analysis of the mitotic events in the video. Before undergoing a division, cells modify their shape, reducing their size and becoming more elliptical, and increasing their brightness. Cell shape variations during mitotic processes are characterized in the literature [35]. The theoretical reason for the relationship between cell brightness increases and the start of mitotic processes was not as clear. After a review of the literature, it was found that chromatin present in cell nuclei, which takes its structure due to attachment to H2B histones, undergoes restructurings during mitosis [36, 37]. In the real *in vitro* experiment used, the authors used mCherry-labeled H2B histones, which are present in the nuclei and therefore allow for

clear identification of the nuclei. These histones have been extensively used as fluorescent markers [38]. Thus, it is clear that the increase in brightness is related to the movements of chromatin in the cell, which can be closely related to the start of mitosis.

Thus, this model makes use of the same features (in addition to additional characteristics of the cell) obtained during the feature extraction process to predict mitotic events. This analysis is embedded in the framework described in the present work since these events are known to be related to the energetic cycles of the cells. In this case, a different part of the energetic state of the cell is used for cellular division instead of motility, which motivates the inclusion of this architecture in the present theoretical model.

The model has 4 hidden layers with sizes $48, 96, 64$ and 32, and as the chosen activation function has also been tanh, the inputs have also been normalized to the range $[-1, 1]$ using Equation 15. This model outputs two probabilities (ranging from 0 to 1), for a positive or negative mitotic event. Since it can be considered a classification problem, the activation function for the last layer has been Softmax, which is better suited for binary and multiclass classification tasks. This activation function tends to maximize the probability for one of the classes and minimize it for the rest of them.

Mitosis probabilities are predicted for every frame in the trajectory with no further restrictions, to force the model to learn the dynamics of these processes, which usually extend for more than 1 frame. As frames with mitotic events have a value of 1 for the ground truth and frames without mitosis have a value of 0, the loss function has been calculated with a Binary Cross Entropy (BCE) loss, which is adequately suited for binary classification problems [39]. Mitosis events have been labeled manually.

3. Experiments and results

This section includes the results for the prediction of trajectories in the three cases (both artificial and real) and predictions of mitosis events in the real experiment.

In-silico cases were created by simulating the movement of rigid circular two-dimensional bodies along a channel 300 pixels wide and 100 pixels high. This movement was stimulated in Python by an imposed velocity increase of 0.05 pixels per frame in every frame for the horizontal dimension and a 0.005 pixel per frame increase in the vertical dimension. A sequence of 100 frames was simulated. Conditions were applied to avoid overlapping of

simulated cells, and all collisions were considered elastic. Data for the first case (cell position along the entire trajectory) were obtained numerically. A second Gaussian noise experiment was included in the extracted positions, and the resulting velocities and characteristics were calculated using these new positions. The aim of these artificial cases was to train the model on progressively complex and variant data.

Regarding the *in vitro* experiment, a video from Marel et al. [40] study on diffusive and density guided cell movement was used. Visual data from the experiment carried out by the authors to test their mathematical model was available in the additional data section. This video shows a time lapse (190 seconds) of Madine-Darby canine kidney cells (MDCK) moving along a two-dimensional channel. They used bright-field and fluorescence microscopy, which provided high visibility of cell nuclei and borders, which was considered a main factor in training the model on a clear dataset. The authors designed the experiment to force the two-dimensional movement of the cells to be in a predominant direction by creating narrow PEG-DMA microchannels. Cells were cultivated on a Petri dish surrounded by these channels, which were kept inaccessible. The channels were then opened, which triggered the movement of cells towards regions with lower density. In contrast with artificially created cases, cell position was not known as data beforehand. In order to obtain said data, a staged process of image segmentation for cell detection and object tracking for trajectory determination was proposed. Further processing of position and trajectory data was required to obtain environmental features that would be used as input to the MLP (also for artificial cases). Thus, the entire process could be divided into the following stages: image segmentation, cell tracking, data processing, ASPNN model, and mitosis prediction model. Only data processing and the ASPNN model apply to artificial cases.

3.1. In-silico determistic experiment

The first artificial case is the simplest, since cell movement is only guided by a two-dimensional gradient without any noise. This deterministic experiment only includes an underlying equation for the movement of cells, thus being completely deterministic. By processing the data with the GENERIC architecture, the model is able to correctly infer this underlying mechanism for movement.

Since the trajectories are simple, there is a clear path towards loss minimization, which has encouraged the use of high learning rates that allow the

SPNN architecture to reach a close prediction in a reduced number of epochs. Moreover, weights in the final MLP layer were initialized manually so that the SPNN architecture was taken as the dominant input. The learning rates for each of the parts of the model and their learning rate scheduler parameters are shown in Table 4. As for MLP, its lesser importance has guided the use of lower learning rates and slower reductions.

Table 4: Training parameters for the first artificial case. LR Scheduler epochs show the number of epochs between each update of the learning rate, which is carried out by multiplying the current learning rate by γ.

Model	**LR**	**LR Scheduler epochs**	**LR Scheduler γ**
SPNN	$1 \cdot 10^{-2}$	500	0.1
MLP	$1 \cdot 10^{-3}$	500	0.2
Final MLP Layer	$1 \cdot 10^{-2}$	500	0.1

The learning process has been successful, with losses for both data and degeneracy conditions decreasing over epochs (see Figure 3). The model has shown high accuracy for the velocities of 90.9% and 96.8% for the coordinates x and y. The lower value for accuracy in the x coordinate could be caused by the higher gradient in this direction. This accuracy has been calculated by using the relative error,

$$Acc = 100 \cdot (1 - |\frac{v_{pred} - v_{gt}}{v_{gt}}|) \ , \tag{16}$$

where v represents velocities. These high values are corroborated by the resulting trajectories, with two examples shown in Figure 4.

Moreover, the correct trajectory predictions have been combined with compliance with the thermodynamical properties, as shown in Figure 5. The total energy is not exactly constant but does not show an increasing tendency, while entropy only grows throughout the trajectory.

Since environmental conditions do not influence movement in this case, SPNN is the main output producer. Figure 6 shows the contribution to the production of output of each part of the model throughout the trajectory, calculated as the product between the input value to the last neuron and its weights. It is noticeable that the SPNN (GENERIC) carries most of the weight, with the MLP providing slight variations. The SPNN captures the

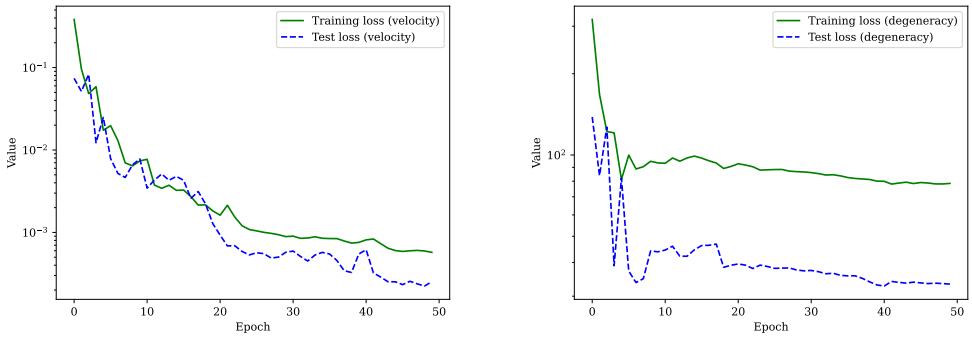

Figure 3: Evolution of loss functions for data (left) and degeneracy conditions (right) for the first artificial case. The horizontal axis represents hundreds of epochs.

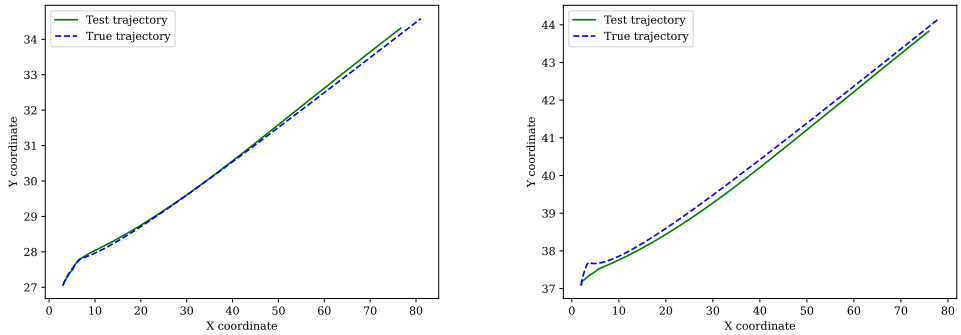

Figure 4: Comparison of two predicted and real trajectories for the first *in-silico* case.

main trend of the velocity of the cells, with the MLP providing a constant offset, which could be understood as an initial velocity.

This first experiment proves that the proposed architecture is able to learn the underlying basic mechanisms for movement relying mostly in the GENERIC-based architecture, stating that the energetic behavior of these bodies is correctly depicted.

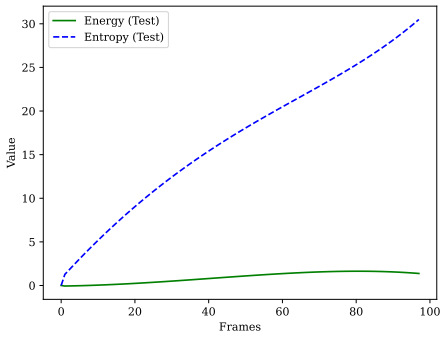

Figure 5: Evolution of thermodynamical variables for a complete trajectory.

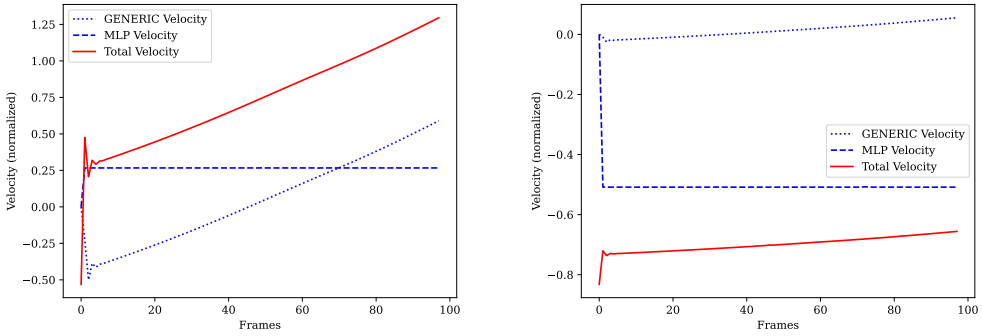

Figure 6: Contribution of each part of the model to the final output velocities for the *in-silico* case without noise. SPNN shows an increasing tendency for both coordinates, while MLP provides variations.

3.2. In-silico case with noise

The second case is very similar to the first one, only including random Gaussian noise to the data obtained from the simulation. The noise distribution had a maximum value of 10% of the current velocity of the cell and was added before calculating new cell positions. As explained before, this case was created to assess the generalization capacity of the model, since real experiment data will be noisy given the accumulated errors and deviations in the image segmentation, tracking, and data processing stages. Thus, initial weights were reduced and learning strategies were more conservatively designed, since the SPNN architecture will not have a clear path towards solution optimization. Training parameters are shown in Table 5.

Table 5: Training parameters for the second artificial case.

Model	**LR**	**LR Scheduler epochs**	**LR Scheduler γ**
SPNN	$1 \cdot 10^{-2}$	500	0.1
MLP	$1 \cdot 10^{-2}$	500	0.1
Final MLP Layer	$1 \cdot 10^{-2}$	500	0.1

The results show that the model was still able to learn and reduce the loss function (see Figure 7), with trajectories being correctly predicted (see Figure 8) and thermodynamical variables evolving adequately (see Figure 9).

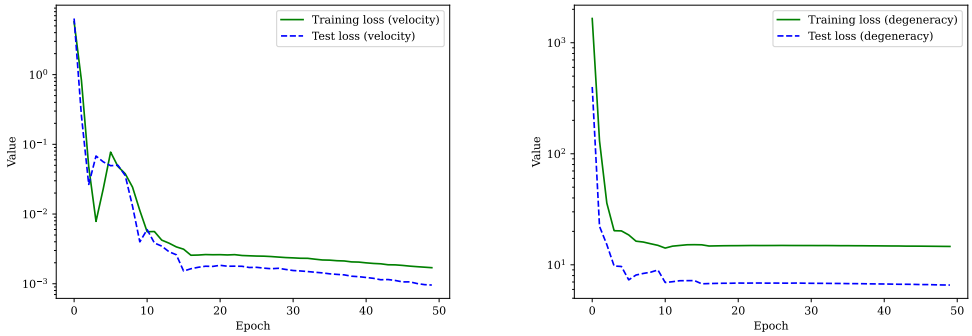

Figure 7: Evolution of loss functions for data (left) and degeneracy conditions (right) for the second artificial case.

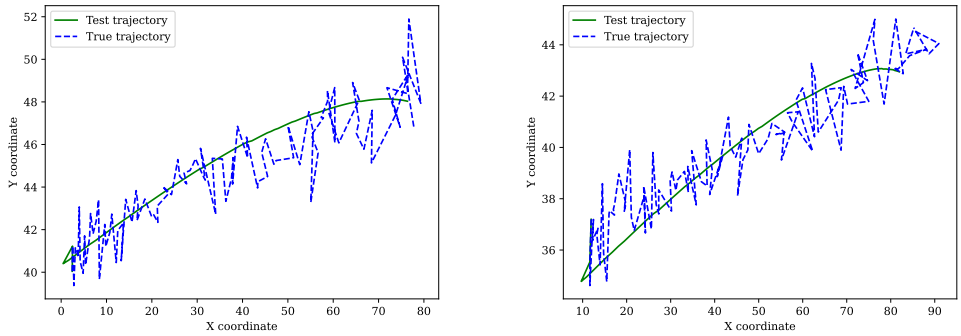

Figure 8: Comparison of two predicted and real trajectories for the second artificial case.

The predicted trajectories do not simulate random variations in the noisy data but follow the same trend and capture the mean movement of the cell, which means that the model is able to correctly extract trajectories from inputs with noise. Even with the high levels of noise that can be appreciated in the true trajectory, the model is capable of filtering that noise and obtaining the mean behavior of the cell.

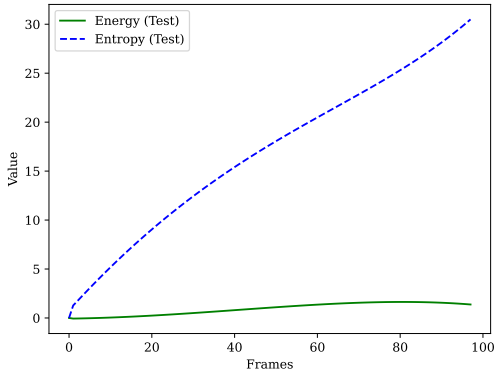

Figure 9: Evolution of thermodynamical variables for a complete trajectory from the second artificial case.

Regarding the contribution of each part of the model to the final velocity output (see Figure 10), a similar behavior to that of the previous case can be appreciated. In this case, in the x axis, SPNN and MLP show a similar contribution, with SPNN capturing the final variations in the trajectory.

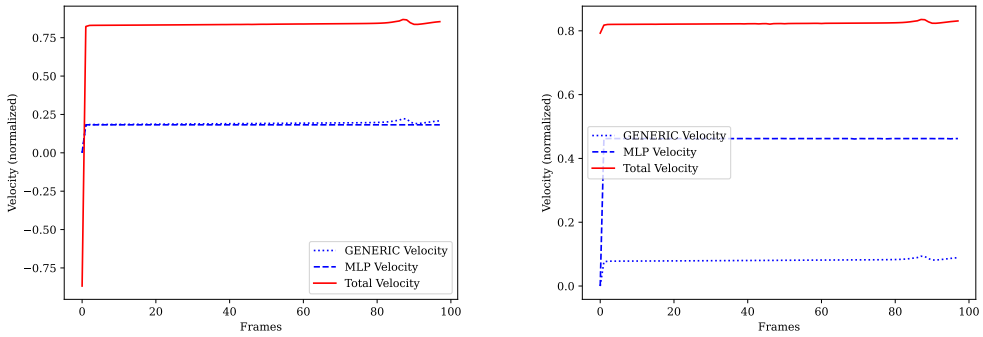

Figure 10: Contribution of each part of the model to the final output velocities for the *in-silico* case with noise. SPNN shows an increasing tendency for both coordinates, while MLP provides variations.

3.3. Real in vitro experiment

Once the performance of the model has been tested on simpler artificial cases, it can be adapted to the real experiment. As the real movement of cells is known to be highly dependent on environmental conditions, the initial weights of the MLP architecture are higher than in artificial cases. In addition, given the higher complexity and variability of real trajectories, the learning rates have been reduced to allow the model to undergo a slower but more confident learning process. Training parameters are shown in Table 6.

Table 6: Training parameters for the real experiment.

Model	**LR**	**LR Scheduler epochs**	**LR Scheduler γ**
SPNN	$5 \cdot 10^{-5}$	100	0.9
MLP	$5 \cdot 10^{-4}$	100	0.9
Final MLP Layer	$5 \cdot 10^{-4}$	100	0.9

The model has shown very efficient learning capabilities, achieving accuracy levels of 91.2% and 95.4% for x and y coordinates, respectively. It is noticeable that the evolution of the loss functions (Figure 11) is much smoother than for the artificial cases and results in an optimized architecture. This shows the validity of reduced learning rates. Trajectories are being correctly predicted (see Figure 12) and accumulated error due to the *roll-out policy* is not a concern, since final positions after 105 frames are sufficiently

close for real and predicted trajectories. In this case, the model is capable of representing velocity variations beyond simple two-dimensional gradients, correctly adapting to a fluctuating movement, especially in the y coordinate, which shows more changes of direction than the x, coordinate, with a clear tendency (left-to-right).

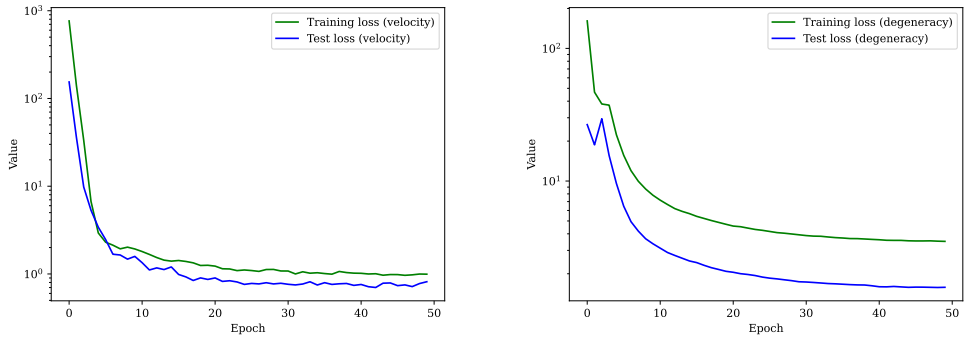

Figure 11: Evolution of loss functions for data (left) and degeneracy conditions (right) for the real experiment.

As stated above, real movements involve a much more complex mechanism. However, the clear trend observed in the x coordinate could be related to the existence of a causing gradient (density gradient, since the right side of the microchannel is empty). The architecture of the complete model can be helpful in detecting which factors have the greatest influence on cell movement. As seen in Figure 13, velocities experience more variations over time (which aligns with real trajectories), and especially variations in MLP velocity are greater than in artificial cases. This reveals a higher importance of MLP input features (environmental conditions) in cell movement. It is noticeable that the MLP is dealing with heterogeneous variations in the trajectory, which could be caused by changing features of the environment (surrounding cells, surface density, internal energetic state of the cell, etc.), while the SPNN maintains a constant contribution that could be related to underlying gradients or movement causes.

In any case, this last analysis further confirms the main idea of this work, which is the need of an additional architecture that accounts for environmental features which are well beyond the Lagrangian behavior of the mechanical system. While the importance of this part of the model was not high, it captures most of the evolution of the system in the real *in-vitro* case. The

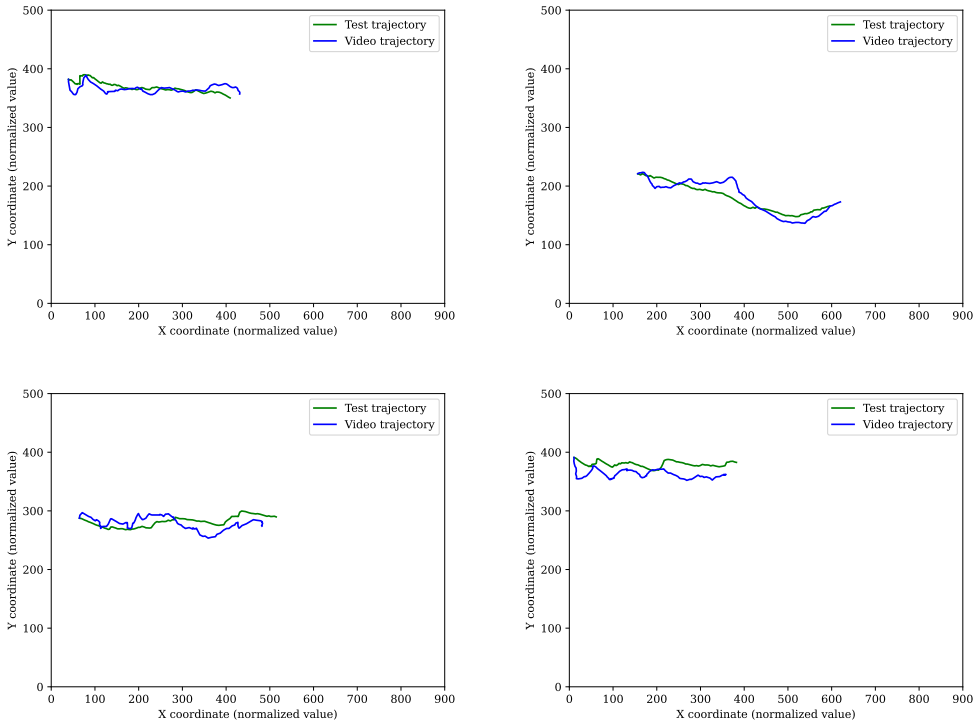

Figure 12: Comparison of four predicted and true trajectories for the real experiment.

GENERIC architecture still shows a non-negligible contribution, which could be further related to constant environmental characteristics influencing cell movement.

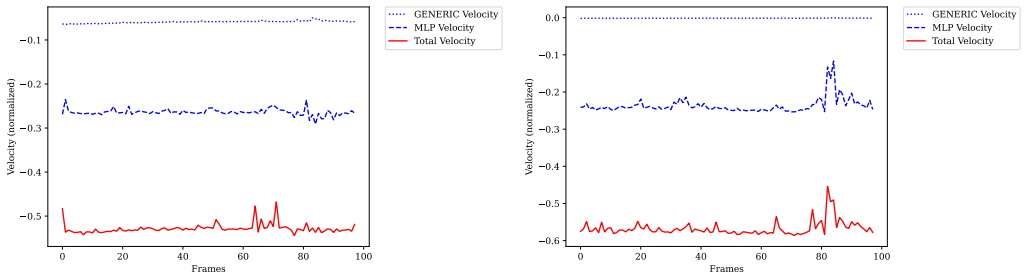

Figure 13: Contribution of each part of the model to the final output velocities for the real experiment.

The model also represents the compliance of the system with thermodynamical principles, with a clear increase in entropy and a stable evolution (although a decreasing tendency can be observed) of total energy, as seen in Figure 14.

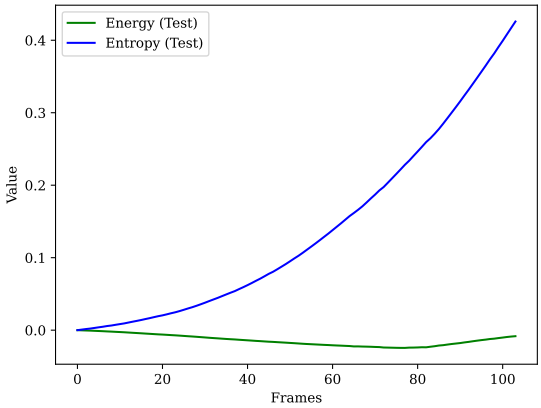

Figure 14: Evolution of thermodynamical variables for a complete trajectory from the real experiment.

3.4. Mitosis prediction

The mitosis prediction model was trained simultaneously with the ASPNN in the real experiment. As explained above, the loss was calculated with BCE function, and the training parameters are shown in Table 7. This model has been trained for 20000 epochs, since preliminary tests showed that 5000 epochs were not sufficient.

Table 7: Training parameters for the mitosis prediction model.

Model	**LR**	**LR Scheduler epochs**	**LR Scheduler γ**
Mitosis	$2 \cdot 10^{-4}$	40000	0.5

As stated before, variations in area and brightness have been considered fundamental inputs for this model. As mitosis processes have an extended duration over several frames, these variations were calculated for frames periods recursively, which means that variations between frames were added for a given frame. Thus, two new parameters were included in the model: the number of previous frames to consider when calculating the area and brightness recurrence. They were set to 2 and 3, recursively, as it was observed that increases in cell brightness began before variations in shape (and area), which is consistent with the description of mitosis processes in the literature [41].

The resulting model has been tested on a set of 30 trajectories with a total of 12 mitotic events. The model was able to correctly learn and reduce the loss function (see Figure 15).

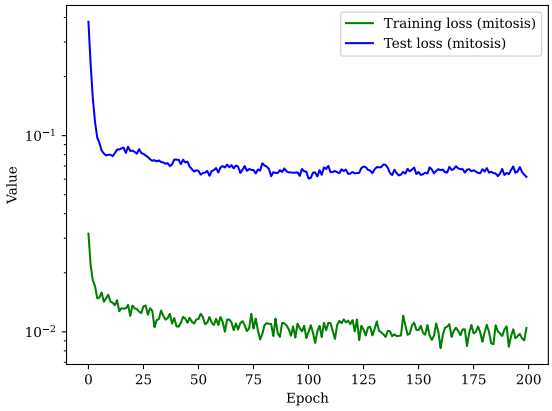

Figure 15: Evolution of loss function for mitosis prediction model.

The model achieved a precision of 69%, defined as correctly predicted positive events out of total positive events, in the test set. An event is correctly predicted if the probability of mitosis in a 6 frame window (3 previous and

3 next frames) centered in the frame with a real mitosis is higher than 0.6 (within the $[0, 1]$ interval). The percentage of false positive predictions was 0.1%, which shows that the model has adequate generalization capabilities and does not trigger easily. Two examples of comparison of model outputs with ground truth data are shown in Figure 16.

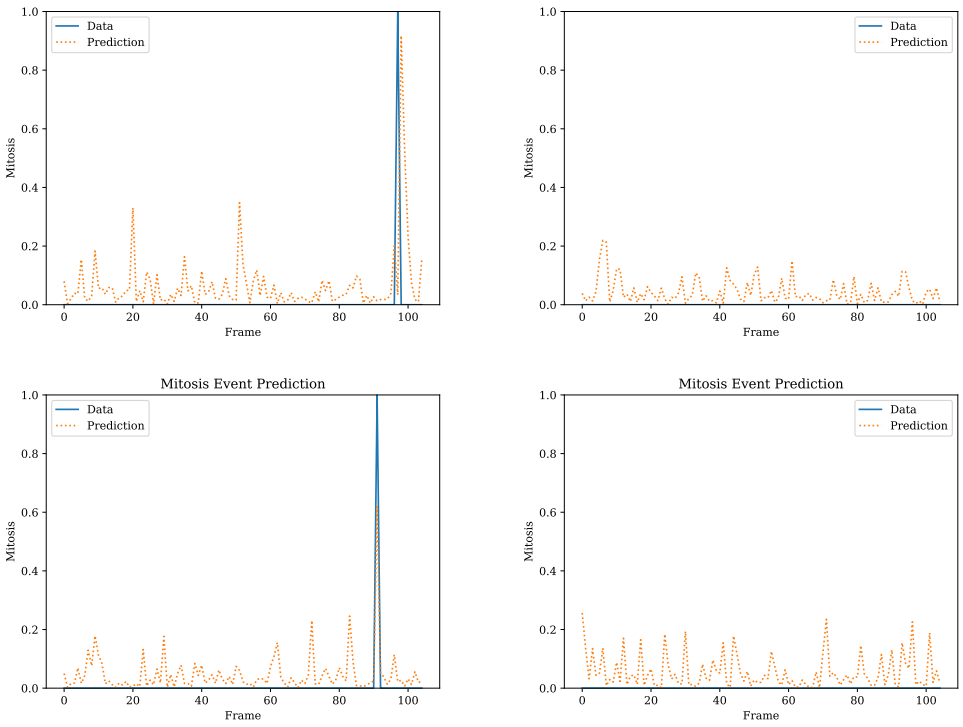

Figure 16: Comparison of model outputs and ground truth data for two trajectories with one mitotic event (left) and two without any mitotic events (right).

4. Conclusions

The presented work provides a new approach to the analysis of cell migration. It proposes a novel framework that recognizes the complexity of biological systems, and specifically cell networks and clusters, which move according to a large number of mechanisms that involve their own state and the environmental conditions of their surroundings. We propose a new tool

for studying many of these factors together, which eliminates the need for complex experiment designs aimed at highlighting a particular feature.

Our Augmented Structural Preserving Neural Network is based on two different parts: an SPNN and an MLP architecture. These two parts each focus on a part of the biological problem. While the SPNN studies the movement of cells as purely mechanical objects which must comply with thermodynamical principles, the MLP accounts for existing patterns in cell behavior that might be a response to its surroundings. The first one only takes positional and velocity parameters as inputs, while the second one uses a set of environmental characteristics that can be extracted from the visual analysis of cell movement in a video. In order to obtain these data, Computer Vision techniques involving image segmentation (SAM model) for cell detection and object tracking for trajectory determination (DeepOCSort) have been used to obtain cell positions over time, which have later been processed to obtain environmental conditions for each cell in each frame. The combined use of these two architectures with different inputs can also provide insight into the influence of each set of inputs on cell movement.

The model has been tested on three cases with an increasing degree of complexity: an artificial case without noise, an artificial case with noise, and a real *in vitro* experiment. For all three cases, velocity accuracies have exceeded 85% in both coordinates, with higher values in the first artificial case and the real experiment. Analysis of trajectories has shown that the accumulated error due to the *roll-out* policy is not a major concern. Moreover, compliance with thermodynamical principles has also been demonstrated.

Lastly, we present a mitosis event prediction model based on an MLP architecture that uses the same visually observed features as the ASPNN as inputs. This model has achieved 69% accuracy, which reveals that mitosis prediction is possible. Future lines of work should more deeply analyze this possibility, as being able to foresee cell division and proliferation mechanics could represent a major advance in the understanding of many biological processes or pathologies.

5. Acknowledgements

Grant PID2021-126051OB-C43 funded by MCIN/AEI/ 10.13039/ 501100011033 and “ERDF A way of making Europe”.

References

[1] R. Horwitz, D. Webb, Cell migration, Current Biology 13 (19) (2003) R756–R759.

[2] S. Kurosaka, A. Kashina, Cell biology of embryonic migration, Birth Defects Research Part C: Embryo Today: Reviews 84 (2) (2008) 102–122.

[3] P. Friedl, D. Gilmour, Collective cell migration in morphogenesis, regeneration and cancer, Nature reviews Molecular cell biology 10 (7) (2009) 445–457.

[4] P. Torres, M. Castro, M. Reyes, V. Torres, Histatins, wound healing, and cell migration, Oral diseases 24 (7) (2018) 1150–1160.

[5] W. J. Polacheck, I. K. Zervantonakis, R. D. Kamm, Tumor cell migration in complex microenvironments, Cellular and Molecular Life Sciences 70 (2013) 1335–1356.

[6] J. Wu, Z. Mao, H. Tan, L. Han, T. Ren, C. Gao, Gradient biomaterials and their influences on cell migration, Interface focus 2 (3) (2012) 337–355.

[7] D. Dormann, C. J. Weijer, Chemotactic cell movement during development, Current opinion in genetics & development 13 (4) (2003) 358–364.

[8] P. A. Iglesias, P. N. Devreotes, Navigating through models of chemotaxis, Current opinion in cell biology 20 (1) (2008) 35–40.

[9] C.-L. Hu, F. S. Barnes, A theory of necrotaxis, Biophysical Journal 10 (10) (1970) 958–969.

[10] X. Trepat, J. J. Fredberg, Plithotaxis and emergent dynamics in collective cellular migration, Trends in cell biology 21 (11) (2011) 638–646.

[11] N. Gjorevski, A. S. Piotrowski, V. D. Varner, C. M. Nelson, Dynamic tensile forces drive collective cell migration through three-dimensional extracellular matrices, Scientific reports 5 (1) (2015) 11458.

[12] M. R. Amieva, H. Furthmayr, Subcellular localization of moesin in dynamic filopodia, retraction fibers, and other structures involved in substrate exploration, attachment, and cell-cell contacts, Experimental Cell Research 219 (1) (1995) 180–196.

[13] L. Saucedo-Mora, M. Á. Sanz, F. J. Montáns, J. M. Benítez, A simple agent-based hybrid model to simulate the biophysics of glioblastoma multiforme cells and the concomitant evolution of the oxygen field, Computer Methods and Programs in Biomedicine 246 (2024) 108046.

[14] E. M. Benetti, M. K. Gunnewiek, C. A. van Blitterswijk, G. J. Vancso, L. Moroni, Mimicking natural cell environments: design, fabrication and application of bio-chemical gradients on polymeric biomaterial substrates, Journal of Materials Chemistry B 4 (24) (2016) 4244–4257.

[15] S. Malijauskaite, S. Connolly, D. Newport, K. McGourty, Gradients in the in vivo intestinal stem cell compartment and their in vitro recapitulation in mimetic platforms, Cytokine & Growth Factor Reviews 60 (2021) 76–88.

[16] T. M. Keenan, A. Folch, Biomolecular gradients in cell culture systems, Lab on a Chip 8 (1) (2008) 34–57.

[17] S. Rafieyan, E. Vasheghani-Farahani, N. Baheiraei, H. Keshavarz, Mlate: Machine learning for predicting cell behavior on cardiac tissue engineering scaffolds, Computers in Biology and Medicine 158 (2023) 106804.

[18] F. M. Garcia-Moreno, J. Ruiz-Espigares, M. A. Gutiérrez-Naranjo, J. A. Marchal, Using deep learning for predicting the dynamic evolution of breast cancer migration, Computers in Biology and Medicine 180 (2024) 108890.

[19] J. Colen, M. Han, R. Zhang, S. A. Redford, L. M. Lemma, L. Morgan, P. V. Ruijgrok, R. Adkins, Z. Bryant, Z. Dogic, et al., Machine learning active-nematic hydrodynamics, Proceedings of the National Academy of Sciences 118 (10) (2021) e2016708118.

[20] M. Mak, C. A. Reinhart-King, D. Erickson, Microfabricated physical spatial gradients for investigating cell migration and invasion dynamics, PLoS one 6 (6) (2011) e20825.

[21] S. Schlie, M. Gruene, H. Dittmar, B. N. Chichkov, Dynamics of cell attachment: adhesion time and force, Tissue Engineering Part C: Methods 18 (9) (2012) 688–696.

[22] K. Webb, V. Hlady, P. A. Tresco, Relationships among cell attachment, spreading, cytoskeletal organization, and migration rate for anchorage-dependent cells on model surfaces, Journal of Biomedical Materials Research: An Official Journal of The Society for Biomaterials and The Japanese Society for Biomaterials 49 (3) (2000) 362–368.

[23] Y. Mao, L. Han, Z. Yin, Cell mitosis event analysis in phase contrast microscopy images using deep learning, Medical image analysis 57 (2019) 32–43.

[24] P. Delgado-Rodriguez, R. M. Sánchez, E. Rouméas-Noël, F. Paris, A. Munoz-Barrutia, Automatic classification of normal and abnormal cell division using deep learning, Scientific Reports 14 (1) (2024) 14241.

[25] A. Szabó, R. M. Merks, Cellular potts modeling of tumor growth, tumor invasion, and tumor evolution, Frontiers in oncology 3 (2013) 87.

[26] A. Kirillov, E. Mintun, N. Ravi, H. Mao, C. Rolland, L. Gustafson, T. Xiao, S. Whitehead, A. C. Berg, W.-Y. Lo, P. Dollár, R. Girshick, Segment anything, arXiv:2304.02643 (2023).

[27] G. Bradski, The OpenCV Library, Dr. Dobb's Journal of Software Tools (2000).

[28] S. van der Walt, J. L. Schönberger, J. Nunez-Iglesias, F. Boulogne, J. D. Warner, N. Yager, E. Gouillart, T. Yu, the scikit-image contributors, scikit-image: Image processing in python, PeerJ 2 (2014) e453. doi:10.7717/peerj.453.

[29] G. Maggiolino, A. Ahmad, J. Cao, K. Kitani, Deep oc-sort: Multi-pedestrian tracking by adaptive re-identification, arXiv preprint arXiv:2302.11813 (2023).

[30] J. Cao, X. Weng, R. Khirodkar, J. Pang, K. Kitani, Observation-centric sort: Rethinking sort for robust multi-object tracking, arXiv preprint arXiv:2203.14360 (2022).

[31] H. C. Öttinger, M. Grmela, Dynamics and thermodynamics of complex fluids. ii. illustrations of a general formalism, Physical Review E 56 (6) (1997) 6633.

[32] I. Romero, Thermodynamically consistent time-stepping algorithms for non-linear thermomechanical systems, International journal for numerical methods in engineering 79 (6) (2009) 706–732.

[33] Q. Hernández, A. Badías, D. González, F. Chinesta, E. Cueto, Structure-preserving neural networks, Journal of Computational Physics 426 (2021) 109950.

[34] S. Falkner, A. Klein, F. Hutter, Bohb: Robust and efficient hyperparameter optimization at scale, in: International conference on machine learning, PMLR, 2018, pp. 1437–1446.

[35] M. Thery, M. Bornens, Cell shape and cell division, Current opinion in cell biology 18 (6) (2006) 648–657.

[36] T. Ito, Role of histone modification in chromatin dynamics, The journal of biochemistry 141 (5) (2007) 609–614.

[37] A. S. Belmont, S. Dietzel, A. C. Nye, Y. G. Strukov, T. Tumbar, Large-scale chromatin structure and function, Current opinion in cell biology 11 (3) (1999) 307–311.

[38] V. Giancotti, S. Brovedan, M. Fonda, R. Grandinetti, E. Russo, Intrinsic and extrinsic fluorescence of histones h2a and h2b: a conformational study, Biophysical Chemistry 7 (4) (1978) 269–277.

[39] U. Ruby, V. Yendapalli, Binary cross entropy with deep learning technique for image classification, Int. J. Adv. Trends Comput. Sci. Eng 9 (10) (2020).

[40] A.-K. Marel, M. Zorn, C. Klingner, R. Wedlich-Söldner, E. Frey, J. O. Rädler, Flow and diffusion in channel-guided cell migration, Biophysical journal 107 (5) (2014) 1054–1064.

[41] A. B. Georgi, P. T. Stukenberg, M. W. Kirschner, Timing of events in mitosis, Current biology 12 (2) (2002) 105–114.